EPJ manuscript No.
(will be inserted by the editor)

Neutron Density Distributions of Neutron-Rich Nuclei Studied with the Isobaric Yield Ratio Difference

Chun-Wang MA, Xiao-Man BAI, Jiao YU, and Hui-Ling WEI

Institute of Particle and Nuclear Physics, Henan Normal University, Xinxiang 453007 China

Received: date / Revised version: September 10, 2014

Abstract. The isobaric yield ratio difference (IBD) between two reactions of similar experimental setups is found to be sensitive to nuclear density differences between projectiles. In this article, the IBD probe is used to study the density variation in neutron-rich ^{48}Ca. By adjusting diffuseness in the neutron density distribution, three different neutron density distributions of ^{48}Ca are obtained. The yields of fragments in the 80A MeV ^{40,48}Ca + ^{12}C reactions are calculated by using a modified statistical abrasion-ablation model. It is found that the IBD results obtained from the prefragments are sensitive to the density distribution of the projectile, while the IBD results from the final fragments are less sensitive to the density distribution of the projectile.

PACS. 21.65.Cd Asymmetric matter, neutron matter – 21.65.Ef Symmetry energy – 25.70.Mn Projectile and target fragmentation

arXiv:1408.5617v2 [nucl-th] 9 Sep 2014

1 Introduction

Nuclear symmetry energy (NSE) is one of the hottest questions in the area of heavy-ion collisions (HICs). The yield of a fragment is mainly determined by the free energy of a fragment, the chemical potential properties of the source, and temperature in HICs above the intermediate energy [1,2,3,4,5,6,7]. In the many probes to determine the NSE, the isobaric yield ratio (IYR) [2,3,8,9,10,11,12] can provide cancelation for special energy terms in the free energy of a fragment. Huang *et al.* proposed the IYR method to determine the symmetry energy coefficients of the nearly symmetric fragments [8], and this IYR method was extended to the neutron-rich fragment to understand the evolution of symmetry-energy coefficient in neutron-rich nuclei [13,14,15]. The IYR method is further developed, and improvements have been achieved to understand the IYR results [16,17,18,19,20,21]. The results of the NSE in Refs. [3,8,22,23,24] show a large difference, but the NSE results determined by the isoscaling (IS) method (which uses isotopic or isotonic ratios in HICs) and the isobaric yield ratio difference (IBD) method are found to be similar [17,18]. Besides, the IYR is also introduced to determine the temperature of heavy fragments by using different approximations for the free energy of fragments [6,7,25].

The IBD is found to be sensitive to nuclear density [17,18,26]. The IBD, which is defined as the differences between the IYRs in two reactions of similar experimental setups, is found sensitive to nuclear density difference between projectiles. The IBD is defined as,

$$\begin{aligned} \Delta\mu_{21}/T &= \ln[\tfrac{\sigma_2(A,I+2)}{\sigma_2(A,I)}] - \ln[\tfrac{\sigma_1(A,I+2)}{\sigma_1(A,I)}], \\ &= [\mu_{n2} - \mu_{n1} - (\mu_{p2} - \mu_{p1})]/T, \\ &= (\Delta\mu_{n21} - \Delta\mu_{p21})/T, \end{aligned} \quad (1)$$

where μ_n (μ_p) denotes the chemical potential of neutrons (protons), which depends on both neutron (proton) density and temperature [27,28,29]; T is the temperature; $\sigma(A,I)$ is the cross section of the fragment (A,I) with $I(=N-Z)$. Indexes 1 and 2 denote the reactions. $\Delta\mu_{21}/T$ is named as the IBD–$\Delta\mu_{21}/T$. The probes based on μ_n (μ_p) are found to be sensitive to NSE, for example, the isoscaling parameters $\alpha \equiv \Delta\mu_{n21}/T$ and $\beta \equiv \Delta\mu_{p21}/T$ [3, 27,30,31,32,33]. In theory, $\Delta\mu_{21}/T = \alpha - \beta$, and this has been proved in fragments showing the isoscaling phenomena [17,18]. α (β) is also correlated to the relative neutron (proton) density between reactions, which is $e^\alpha = \hat{\rho}_n = \frac{\rho_{n,2}}{\rho_{n,1}}$ ($e^\beta = \hat{\rho}_p = \frac{\rho_{p,2}}{\rho_{p,1}}$). [27,28,29]. Equivalently, $\alpha = \ln\rho_{n,2} - \ln\rho_{n,1}$ ($\beta = \ln\rho_{p,2} - \ln\rho_{p,1}$) denoting the difference between the density of neutrons (protons).

A neutron-rich nucleus has a neutron-skin due to the large difference between its ρ_n and ρ_p distributions. The neutron-skin thickness is also one of the important parameters to study the NSE of the sub-saturation nuclear matter, but there are some difficulties in measuring the neutron-skin thickness [34,35,36,37,38,39,40,41,42,43,44]. In this article, we study the sensitivity of the IBD probe to the neutron density variation in ^{48}Ca. In general, the quantum molecular dynamical (QMD) model [45,46,47, 48] (or its improved versions) and the antisymmetric molecular dynamical (AMD) model [49,50,51,52,53], in which

Send offprint requests to: C.-W. MA: machunwang@126.com

the evolution of reaction can be described, are usually adopted to simulate HICs. Most works using QMD concentrate on the study of the phenomena involving light particles [54,55,56,57,58,59,60,61,62,63,64,65]. For fragment with larger mass, QMD cannot well reproduce the isotopic or isobaric yield distributions. Though AMD predicts the yields of fragments much better than QMD [8,66, 11,**?**], it needs a lot of time to gather enough events [8]. Besides the QMD and AMD models, the constrained molecular dynamics (CoMD) model may also be a good choice since CoMD cost less time than AMD, at the same time, CoMD can predict the yields of fragments well [68,69,70, 71,72]. In the IBD analysis, the yield of fragment with large mass is needed, which can not be easily fulfilled by QMD and AMD. A modified statistical abrasion-ablation (SAA) model, which can well reproduce the yield of fragment [73,74,75,76], is adopted in this work. The proton and neutron density distributions are distinguished in the SAA model [75,76,77,78], which make it easy to change the density distribution. The SAA model will be briefly described in Sec. 2. The IBD results are presented and discussed in Sec. 3, and a summary is presented in Sec. 4.

2 Model descriptions

The SAA model has been described in Refs. [73,74,75]. To show the results more clearly, we introduce the model briefly. The SAA model is a two-stage model to describe the HICs above intermediate energies. The first stage is characterized by the abrasion of nucleons in the projectile nucleus, and the hot prefragments are formed in this stage. The second stage is characterized by the evaporation of light particles (n, p, α), in which the hot prefragment decay to final fragments. The projectile and target nuclei are assumed to be composed of interacting tubes. Omitting the transverse motion of nucleons in the tube, the collisions are described by independent interactions of tube pairs. Assuming the tube to be infinitesimal, the average absorbed mass in a tube at a given impact parameter $\boldsymbol{b}$ is,

$$< \Delta A(b) >= \int d^2s\rho_n^P(\boldsymbol{s})[1 - t_n(\boldsymbol{s}-\boldsymbol{b})] + \int d^2s\rho_p^P(\boldsymbol{s})[1 - t_p(\boldsymbol{s}-\boldsymbol{b})], \quad (2)$$

where $t_k(\boldsymbol{s}-\boldsymbol{b})$ $(k = n, p)$ is the transmission probability for neutrons (protons) at $\boldsymbol{b}$, and is given by,

$$t_k(\boldsymbol{s}-\boldsymbol{b}) = \exp\{-[\rho_n^T(\boldsymbol{s}-\boldsymbol{b})\sigma_{nk} + \rho_p^T(\boldsymbol{s}-\boldsymbol{b})\sigma_{pk}]\}, \quad (3)$$

where ρ^T is the nuclear-density distribution of the target integrated along the beam direction, $\boldsymbol{s}$ and $\boldsymbol{b}$ are defined in the plane perpendicular to the beam, and $\sigma_{k'k}$ are the nucleon-nucleon reaction cross sections. It is easy to see that the yield of a prefragment is decided by the nuclear density distribution and $\sigma_{k'k}$. The yield for a specific prefragment, which has ΔN of neutrons and ΔZ of protons removed from the projectile, is calculated as follows,

$$\sigma(\Delta N, \Delta Z) = \int d^2bP(\Delta N, b)P(\Delta Z, b), \quad (4)$$

where $P(\Delta N, b)$ $[P(\Delta Z, b)]$ is the probability distribution for the abraded neutrons (protons) at a given b. These probability distributions are a superposition of different binomial distributions for all the tubes.

The Fermi-type density distribution is adopted for ρ_n (ρ_p) [79],

$$\rho_k(r) = \frac{\rho_k^0}{1 + \exp(\frac{r-C_k}{t_k f_k/4.4})}, \quad k = n, p \quad (5)$$

where ρ_k^0 is a normalization constant, t_k is the diffuseness parameter, and C_k is the radius of the half density for the neutron (proton) density distribution. f_k is introduced to change the diffuseness and the neutron-skin thickness of a nucleus [41,42,43,44,80,81]. If $f_k = 1$, Eq. (5) is the original Fermi-type density distribution.

The evaporation of a prefragment is calculated by using a conventional statistical model assuming the thermal equilibrium [73,74]. The statistical hole-energy model gives an average excitation energy of 13.3MeV per hole (due to abrasion). The excitation energy of a prefragment is $E^* = 13.3 < A(b) >$MeV, with $< A(b) >$ being the average abraded numbers of nucleons from the projectile. By using the Weiszäcker-Bethe mass formula [82,83], the binding energy of nuclei (A, Z), (A-1, Z-1), (A-1, Z) and (A-4, Z-2) are calculated, from which the separation energy of neutron (S_n), proton (S_p) and α (S_α) of the nucleus (A, Z) can be decided. For a prefragment with E^*, the most possible particle emitted is chosen according to $\min(S_n, S_p, S_\alpha)$. The evaporation stops when the excitation energy falls below the lowest particle threshold of the residual nucleus. This is an economical decay method compared to the sequential decay method GEMINI [84] or the statistical multifragmentation model (SMM) [85]. Similar methods have been adopted in works dealing with the clusterization in the framework of the QMD model [86, 87,88]. After the evaporation, the yield of the final fragment can be obtained. The SAA model can well predict the yields of fragments in the 140A MeV ^{40,48}Ca + ^{9}Be and ^{58,64}Ni + ^{9}Be reactions [77,78,89].

3 Results and discussion

The yields of fragments in the 80A MeV ^{40,48}Ca + ^{12}C reaction are calculated. For ^{48}Ca, $f_n = 1$, 2 and 3 are adopted. The ^{40}Ca reaction is labeled as 1, and the ^{48}Ca reactions with a different f_n are labeled as 2. Since $\Delta\mu_{21}/T$ denotes the difference between the projectiles, we first discuss the difference between ρ_n (ρ_p) of ^{40}Ca and ^{48}Ca, which are plotted in Fig. 1. The ρ_p distributions of ^{40}Ca and ^{48}Ca are very similar, thus the difference between them will not be considered. For ^{48}Ca, more neutrons are pushed to the skirt region from the core with increasing f_n resulting in the decrease of ρ_n in the core and making the

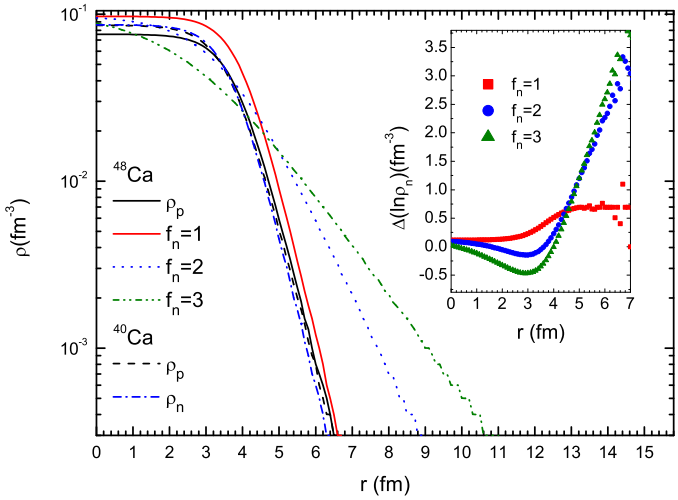

Fig. 1. (Color online) The neutron and proton density distributions of ^{40}Ca and ^{48}Ca according Eq. (5). For ^{48}Ca, f_n =1, 2, and 3 are plotted. In the inserted figure, the difference between the neutron density distributions [$\Delta(\ln\rho_n)$] of ^{40}Ca and ^{48}Ca are plotted, in which $\Delta(\ln\rho_n) = \ln\rho_n(^{48}Ca) - \ln\rho_n(^{40}Ca)$. r denotes the nuclear radius.

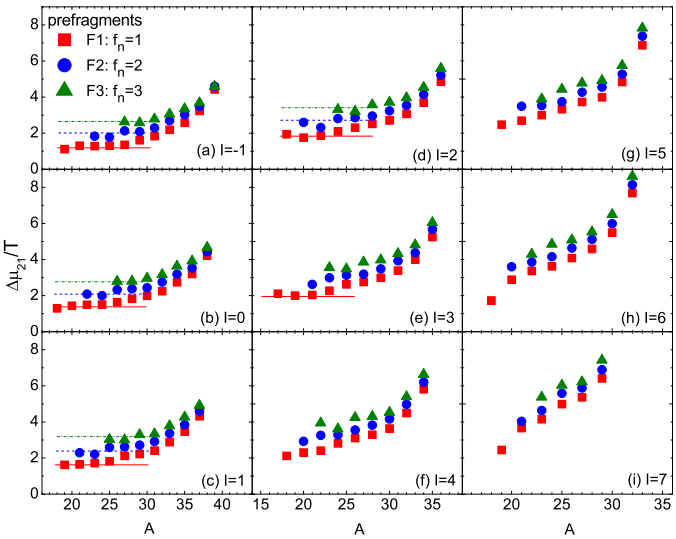

Fig. 2. (Color online) $\Delta\mu_{21}/T$ determined from the prefragments produced in the calculated 80A MeV ^{48,40}Ca + ^{12}C reactions. The squares, circles and triangles denote the results for f_n = 1, 2, and 3 in the ^{48}Ca neutron density distribution, respectively. From panel (a) to (i), the results are obtained from the prefragments with I from -1 to 7. The lines denote the plateaus in the $\Delta\mu_{21}/T$ distributions.

neutron-skin thicker. In the inserted figure of Fig. 1, the results of $\Delta(\ln\rho_n) = \ln\rho_n(^{48}Ca) - \ln\rho_n(^{40}Ca)$ are plotted. For f_n =1, $\Delta(\ln\rho_n)$ is similar ($\sim$ 0) when r<3 fm, but increases with r in the range 3< r <4.5 fm, and becomes similar again when r > 4.5 fm. For f_n =2 and 3, $\Delta(\ln\rho_n)$ first decreases with the increasing r when r <$\sim$3.2 fm, then increases fast with r almost linearly.

The yield of a prefragment is determined by the ρ_n and ρ_p distributions according to Eq. (3), thus the probe constructed from prefragments is supposed to reflect the density changes directly. It is concluded that $\Delta\mu_{21}/T$ is sensitive to the difference between the ρ_n of isotopic projectiles. The results of the IBD–$\Delta\mu_{21}/T$ are obtained by using the yields of prefragments and final fragments in the ^{48,40}Ca reactions. For clarity, the $\Delta\mu_{21}/T$ for ^{48}Ca with f_n = 1, 2, and 3 are labeled as F1, F2, and F3, respectively. The $\Delta\mu_{21}/T$ determined from the prefragments are plotted in Fig. 2. When I < 3, the $\Delta\mu_{21}/T$ in the prefragment with a relatively small A form plateaus, while $\Delta\mu_{21}/T$ increases with A in the large A fragments. When I > 3, the plateau of $\Delta\mu_{21}/T$ disappears, and $\Delta\mu_{21}/T$ increases with A almost linearly. The plateau in $\Delta\mu_{21}/T$ is explained as the gentle change of ρ_n in the cores of the projectiles, and the height of the plateau in the $\Delta\mu_{21}/T$ distribution is assumed to reflect the difference between ρ_n of the projectiles [17]. For the prefragments with I from -1 to 7, the $\Delta\mu_{21}/T$ shows an obvious regular increase with f_n, which corresponds to the enlarged $\Delta(\ln\rho_n)$ between ^{48}Ca and ^{40}Ca. The plateaus in $\Delta\mu_{21}/T$ of the I = -1, 0, 1 and 2 prefragments also increase with f_n, but the width of the plateau becomes shorter with the increased f_n. The enlarged $\Delta(\ln\rho_n)$ can accounts for the increasing $\Delta\mu_{21}/T$ with f_n, and the increasing $\Delta(\ln\rho_n)$ in the r <3.2 fm explain the disappear of the plateau in the neutron-rich fragments (see the inserted figure in Fig. 1). Compared with the heights of the IBD results ($\approx$ 2) [17] obtained from the measure fragments [90], the heights of the plateaus in F1 are smaller, but those in F2 are similar.

Though the prefragments can well indicate the density change in the projectile, they are not measurable in the experiments. In SAA, the final fragments correspond to the measured ones in experiment. The $\Delta\mu_{21}/T$ determined from the final fragments are plotted in Fig. 3. Most of the prefragments with I > 5 can not survive the evaporation process, thus only the $\Delta\mu_{21}/T$ obtained from the final fragments with I from -1 to 4 are plotted. In the final fragments, the distribution of $\Delta\mu_{21}/T$ is also found increase regularly with f_n. The heights of the plateaus are about 0.5, which are much smaller than the measured results in Ref. [17]. But the heights of the plateaus are larger than those in Ref. [26], which studied the density changes between calcium isotopes (the different f_n makes a larger $\Delta\rho_n$ compared with those in Ref. [26]).

Now the phenomena that $\Delta\mu_{21}/T$ increases with A in the large A fragments will be addressed. In this work, f_p is not changed, thus in theory $\beta = 0$ and $\Delta\mu_{21}/T = \alpha$. The underlying physics of the changing of α with N should suit for that of $\Delta\mu_{21}/T$. The values of α obtained form isotopic ratios of small Z are similar, but changes with Z when Z approximates to that of the projectile. This phenomena is usually explained as that the large Z fragments are produced in the peripheral reactions, which correspond to the surface region of the projectile where $\Delta(\ln\rho_n)$ changes quickly. We have also explained the increasing $\Delta\mu/T$ (or $\alpha-\beta$) with A in a similar way by consider the central and peripheral collisions separately [17,18,26]. The fragments with small A are mainly produced in the central collisions which is almost not influenced by the neutron-skin, while

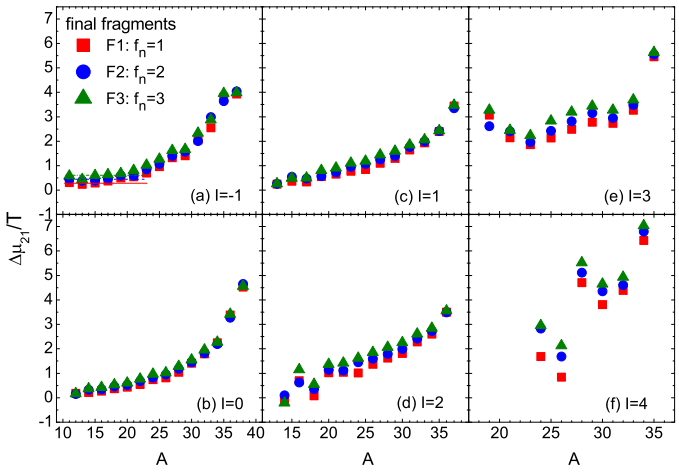

Fig. 3. (Color online) The same as Fig. 2 but for the results determined from the final fragments. From panel (a) to (f), the results are from final fragments with I form -1 to 4. The lines in panel (a) denote the plateaus in the $\Delta\mu_{21}/T$ distributions.

the fragments having A near the projectile are governed by the neutron-skin [20,21,43,80]. The neutron-skin is also found to make the IYR increase nonlinearly [20,21].

At last, we discuss the evaporation effects in $\Delta\mu_{21}/T$. The secondary decay influences the isoscaling result greatly. The isobaric yield distributions and the resultant IYRs can also be largely modified by the decay process [15,26]. Though the IYRs are not compared directly in this work, it is easy to find the mass ranges of the final fragments are larger than those of the prefragments. The $\Delta\mu_{21}/T$ obtained from the final fragments are much smaller than those from the prefragments, and are sensitive to the decrease of f_n, which has been found in the $\Delta\mu_{21}/T$ obtained in the reactions induced by the calcium isotopes [26]. In the decay process, the binding energy of nucleus is used by omitting its temperature dependence. In fact, the binding energy of a light nucleus is influenced much more easily by temperature than that of a heavy nucleus [6], which potentially influence the quality of the SAA model. For fragments in a specific Z-chain produced in the 140A MeV ^{40,48}Ca (^{58,64}Ni) + ^{9}Be reactions [66,90], the yields of the small-A isotopes have relative large errors compared with those of the large-A isotopes [89]. Thus the evaporation in the present SAA model make it difficult to conclude wether the IBD probe is useful in detecting the neutron density in a neutron-rich nucleus. Further investigation of the evaporation effects in the IBD probe is suggested.

4 summary

In summary, the IBD probe is used to study the density change in the neutron-rich ^{48}Ca nucleus. The SAA model is used to calculate the yields of fragments in the 80A MeV ^{40,48}Ca + ^{12}C reactions. f_n = 1, 2 and 3 are adopted to adjust the neutron density distributions in ^{48}Ca. The results of IBD–$\Delta\mu_{21}/T$ are obtained by analyzing the yields of the prefragments and final fragments produced in the ^{40}Ca and ^{48}Ca reactions. The $\Delta\mu_{21}/T$ distribution is explained by using the $\Delta(\ln\rho_n)$ between ^{48}Ca and ^{40}Ca, in which the plateau of $\Delta\mu_{21}/T$ is explained as the gentle change of $\Delta(\ln\rho_n)$ in the core of the projectiles, and the increasing $\Delta\mu_{21}/T$ with A is explained as the enlarged $\Delta(\ln\rho_n)$ between the surface region of the projectiles. The decay process influences the $\Delta\mu_{21}/T$ greatly. The $\Delta\mu_{21}/T$ obtained from prefragments is sensitive to f_n, while the $\Delta\mu_{21}/T$ obtained from the final fragments is less sensitive to f_n. In the present status of the SAA model, it is not easy to conclude whether the IBD probe can be used to detect the density change in a neutron-rich nucleus. In addition, the improvement of evaporation in the SAA model is suggested.

Acknowledgments

This work is supported by the Program for Science & Technology Innovation Talents in Universities of Henan Province (13HASTIT046), and the Young Teacher Project in Henan Normal University.

References

1. R. W. Minich, S. Agarwal, A. Bujak*et al.*, Phys. Lett. B **118**, 458 (1982).
2. M. Huang, A. Bonasera, Z. Chen *et al.*, Phys. Rev. C **81**, 044618 (2011).
3. P. Marini, A. Bonasera, A. McIntosh *et al.*, Phys. Rev. C **85**, 034617 (2012).
4. S. Goyal and R. K. Puri, Phys. Rev. C **83**, 047601 (2011).
5. M. B. Tsang, W. G. Lynch, W. A. Friedman *et al.*, Phys. Rev. C **76**, 041302(R) (2007).
6. C. W. Ma, J. Pu, Y. G. Ma, R. Wada, S. S. Wang, Phys. Rev. C **86**, 054611 (2012).
7. C. W. Ma, X. L. Zhao, J. Pu *et al.*, Phys. Rev. C **88**, 014609 (2013).
8. M. Huang, Z. Chen, S. Kowalski *et al.*, Phys. Rev. C **81**, 044620 (2010).
9. M. Huang, R. Wada, Z. Chen *et al.*, Phys. Rev. C **82**, 054602(R) (2010).
10. C.-W. Ma, F. Wang, Y.-G. Ma, C. Jin, Phys. Rev. C **83**, 064620 (2011).
11. W. Lin, R. Wada, M. Huang *et al.*, Nucl. Sci. Tech. **24**, 050511 (2013).
12. R. Wada, M. Huang, W. Lin *et al.*, Nucl. Sci. Tech. **24**, 050501 (2013).
13. C.-W. Ma, J. Pu, H.-L. Wei *et al.*, Eur. Phys. J. A **48**, 78 (2012).
14. C. W. Ma, J. Pu, S. S. Wang, H. L. Wei, Chin. Phys. Lett. **29**, 062101 (2012).
15. C. W. Ma, H. L. Song, J. Pu *et al.*, Chin. Phys. C **37**, 024102 (2013).
16. C.-W. Ma, S.-S. Wang, Y.-L. Zhang, H.-L. Wei, arXiv:1402.5493 [nucl-th].
17. C. W. Ma, S. S. Wang, Y. L. Zhang, H. L. Wei, Phys. Rev. C **87**, 034618 (2013).
18. C. W. Ma, S. S. Wang, Y. L. Zhang, H. L. Wei, J. Phys. G: Nucl. Part. Phys. **40**, 125106 (2013).

19. S. R. Souza, M. B. Tsang, Phys. Rev. C **85**, 024603 (2012).
20. C. W. Ma, S. S. Wang, H. L. Wei, Y. G. Ma, Chin. Phys. Lett. **30**, 052101 (2013).
21. C. W. Ma, H. L. Wei, Y. G. Ma, Phys. Rev. C **88**, 044612 (2013).
22. P. Marini, A. Bonasera, G. A. Souliotis *et al.*, Phys. Rev. C **87**, 024603 (2013).
23. S. Mallik, G. Chaudhuri, Phys. Rev. C **87**, 011602(R) (2013).
24. S. Mallik, G. Chaudhuri, Phys. Lett. B **727**, 282 (2013).
25. C. W. Ma, C. Y. Qiao, S. S. Wang, F. M. Lu, L. Chen, M. T. Guo, Nucl. Sci. Tech. **24**, 050510 (2013).
26. C. W. Ma, J. Yu, X. M. Bai, Y. L. Zhang, H. L. Wei, S. S. Wang, Phys. Rev. C **89**, 057602 (2014).
27. A. S. Botvina, O. V. Lozhkin, W. Trautmann, Phys. Rev. C **65**, 044610 (2002).
28. M. B. Tsang, W. A. Friedman, C. K. Gelbke, W. G. Lynch, G. Verde, and H. Xu, Phys. Rev. Lett. **86**, 5023 (2001).
29. E. Geraci, M. Bruno, M. D'Agostino *et al.*, Nucl. Phys. A **732**, 173 (2004).
30. M. Huang, Z. Chen, S. Kowalski *et al.*, Nucl. Phys. A **847**, 233 (2011).
31. H. S. Xu *et al.*, Phys. Rev. Lett. **85**, 716 (2000).
32. M. Colonna, Phys. Rev. Lett. **110**, 042701 (2013).
33. Z. Chen, S. Kowalski, M. Huang *et al.*, Phys. Rev. C **81**, 064613 (2010).
34. C. J. Horowitz, Phys. Rev. C **57**, 3430 (1998).
35. X. Roca-Maza, M. Centelles, X. Viñas, M. Warda, Phys. Rev. Lett. **106**, 252501 (2011).
36. S. Abrahamyan et al. (PREX Collaboration), Phys. Rev. Lett. **108**, 112502 (2012).
37. Z. Zhang and L. W. Chen, Physics Letters B **726**, 234 (2013).
38. J. Liu, Z. Ren, T. Dong, Nucl. Phys. A **888**, 45 (2012).
39. J. Liu, Z. Ren, T. Dong, Nucl. Phys. A **900**, 1 (2013).
40. M. B. Tsang, J. R. Stone, F. Camera *et al.*, Phys. Rev. C **86**, 015803 (2012).
41. C. W. Ma, Y. Fu, D. Q. Fang *et al.* Chin. Phys. B **17**, 1216 (2008).
42. D. Q. Fang, Y. G. Ma, X. Z. Cai, W. D. Tian, H. W. Wang, Phys. Rev. C **81**, 047603 (2010).
43. C.-W. Ma, H.-L. Wei, M. Yu, Phys. Rev. C **82**, 057602 (2010).
44. Z. T. Dai, D. Q. Fang, Y. G. Ma, X. G. Cao, G. Q. Zhang, Phys. Rev. C **89**, 014613 (2014).
45. J. Aichelin, Phys. Rep. **202**, 233 (1991).
46. R. K. Puri and J. Aichelin, J. Comp. Phys. **162**, 245 (2000).
47. K. Zbiri et al. (ALADIN Collaboration, INDRA Collaboration), Phys. Rev. C **75**, 034612 (2007).
48. Y. K. Vermani, R. K. Puri, EPL **85**, 62001 (2009).
49. A. Ono, H. Horiuchi, T. Maruyama, A. Ohnishi, Phys. Rev. Lett. **68**, 2898 (1992)
50. A. Ono, H. Horiuchi, Phys. Rev. C **53**, 2958 (1996).
51. A. Ono, Phys. Rev. C **59**, 853 (1999).
52. A. Ono, H. Horiuchi, Prog. Part. Nucl. Phys. **53**, 501 (2004).
53. A. Ono, AIP Conf. Proc. **884**, 292 (2007).
54. B.-A. Li, L.-W. Chen, C. M. Ko, Phys. Rep. **464**, 113 (2008).
55. S. Kumar, Y. G. Ma, G. Q. Zhang, C. L. Zhou, Phys. Rev. C **84**, 044620 (2011).
56. S. Kumar, Y. G. Ma, G. Q. Zhang, Phys. Rev. C **86**, 044616 (2012).
57. J. Pu, J. H. Chen, S. Kumar, Y. G. Ma, C. W. Ma, G. Q. Zhang, Phys. Rev. C **87**, 047603 (2013).
58. C. L. Zhou, Y. G. Ma, D. Q. Fang, and G. Q. Zhang, Phys. Rev. C **88**, 024604 (2013).
59. N. Wang, Z. Li, and X. Wu, Phys. Rev. C **65**, 064608 (2002).
60. Y. Zhang, Z. Li, Phys. Rev. C **71**, 024604 (2005).
61. Y. Zhang, Z. Li, Phys. Rev. C **74**, 014602 (2006).
62. Y. Zhang, P. Danielewicz, M. Famiano, Z. Li, W. G. Lynch, and M. B. Tsang, Phys. Lett. B **664**, 145 (2008).
63. Y. Zhang, Z. Li, K. Zhao *et al.*, Nucl. Sci. Tech. **24**, 050503 (2013).
64. J. Su, F. S. Zhang, Phys. Rev. C **84**, 037601 (2011).
65. J. Su, L. Zhu, W. J. Xie, F. S. Zhang, Phys. Rev. C **85**, 017604 (2012).
66. M. Mocko, M. B. Tsang, D. Lacroix *et al*, Phys. Rev. C **78**, 024612 (2008).
67. X. Liu, W. Lin, R. Wada *et al.*, Phys. Rev. C **90**, 014605 (2014).
68. M. Papa, T. Maruyama, and A. Bonasera, Phys. Rev. C **64**, 024612 (2001).
69. M. Papa, F. Amorini, A. Anzalone, *et al.*, Phys. Rev. C **75**, 054616 (2007).
70. M. Papa, G. Giuliani, A. Bonasera, J. Comput. Phys. **208**, 403 (2005).
71. X. Liu, W. Lin, R. Wada *et al.*, Phys. Rev. C **90**, 014604 (2014).
72. L. Francalanza, U. Abbondanno, F. Amorini *et al.*, Nucl. Sci. Tech. **24**, 050516 (2013).
73. T. Brohm, K. -H. Schmidt, Nucl. Phys. A **569**, 821 (1994).
74. J. J. Gaimard, K. H. Schmidt, Nucl. Phys. A **531**, 709 (1991).
75. D. Q. Fang, W. Q. Shen, J. Feng *et al.*, Phys. Rev. C **61**, 044610 (2000).
76. D. Q. Fang, Y. G. Ma, C. Zhong *et al.*, J. Phys. G: Nucl. Part. Phys., **34**, 2173 (2007).
77. C. W. Ma, H. L. Wei, J. Y. Wang *et al.*, Phys. Rev. C **79**, 034606 (2009).
78. C. W. Ma, H. L. Wei, J. Y. Wang, G. J. Liu, Chin. Phys. B **18**, 4781 (2009).
79. A. Ozawa, T. Suzuki, I. Tanihata, Nucl. Phys. A **693**, 32 (2001).
80. C. W. Ma, H. L. Wei, G. J. Liu, and J. Y. Wang, J. Phys. G: Nucl. Part. Phys. **37**, 015104 (2010).
81. C. W. Ma, S. S. Wang, Chin. Phys. C **35**, 1017 (2011).
82. C. F. von Weizsäcker, Z. Phys. **96**, 431 (1935).
83. H. A. Bethe, R. F. Bacher, Rev. Mod. Phys. **8**, 82 (1936).
84. R.J. Charity, M.A. McMahan, G.J. Wozniak *et al.*, Nucl. Phys. A **483**, 371 (1988).
85. A. S. Botvina and I. N. Mishustin, Phys. Rev. C **63**, 061601(R) (2001).
86. S. Goyal, R. K. Puri, Phys. Rev. C **83**, 047601 (2011).
87. Y. K. Vermani et al., J. Phys. G: Nucl. Part. Phys. **37**, 015105 (2010).
88. R. K. Puri, J. Aichelin, J. Comp. Phys. **162**, 245 (2000).
89. H. L. Wei, C. W. Ma, Acta Phys. Sin. **59**, 5364 (2010) (in Chinese).
90. M. Mocko, M. B. Tsang, L. Andronenko *et al.*, Phys. Rev. C **74**, 054612 (2006).